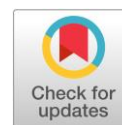


The crystallization of thin Sb_2Te films with vacuum annealing and an electron beam

Anton A. Yushkov*, Vladimir Yu. Kolosov

Institute of Natural Sciences and Mathematics, Ural Federal University, Ekaterinburg 620026, Russia

* Corresponding author: Yushkov.anton@urfu.ru



This paper belongs to a Regular Issue.

Abstract

Thin Sb_2Te films with a thickness gradient were studied via transmission electron microscopy. The processes of forced crystallization were examined with thermal annealing and an electron beam. The crystallization's general tendencies, including competitive nucleation and growth crystallization, were revealed. As the thickness of the sample increases, the size of the crystals growing in the film enlarges. As the temperature increases, the number of crystals in the film grows. Crystallization under the action of an electron beam occurs mainly by nucleation mechanism.

Keywords

Sb_2Te
thin films
phase-change materials
transmission electron microscopy

Received: 24.12.22

Revised: 17.02.23

Accepted: 21.02.23

Available online: 03.03.23

Key findings

- A thin amorphous Sb_2Te film crystallizes in a phase isomorphic to antimony during vacuum annealing.
- During annealing, the processes of nucleation and growth crystallization proceed competitively in the film. As the temperature rises, nucleation predominates.
- The possibility of controlled creation of crystalline regions in an amorphous Sb_2Te film by exposure to a focused electron beam is shown.

© 2022, the Authors. This article is published in open access under the terms and conditions of the Creative Commons Attribution (CC BY) license (<http://creativecommons.org/licenses/by/4.0/>).

1. Introduction

Sb–Te systems, including Sb_2Te and compositions based on it, are considered as perspective thermoelectric materials [1–4]. Characteristic of the amorphous state crystal phase transition in these materials has a critical impact on their properties [5]. The non-linear optical properties of these materials open up prospects for their application in optoelectronics [6–8]. These compositions are also advanced materials for manufacturing non-volatile memory based on the phase transition effect (PCM) [9–15]. The development of multi-level memory cells that are competitive with modern flash memory devices is underway [16, 17]. Unlike other phase-change materials, Sb–Te systems are characterized by a high crystallization rate and thermal stability [13]. The properties of antimony telluride as a topological insulator [18, 19] and a high-temperature superconductor [20] have also been studied.

In order to increase the stability and performance of devices, various dopants are used [12, 13, 15, 21–24]. In

particular, the use of carbon carbide leads to an increase in the crystallization temperature and an increase in the number of PCM memory rewriting cycles [24]. The addition of scandium and yttrium to antimony telluride leads to a reduction in thermal conductivity and an increase in the energy efficiency of PCM devices [23]. The features of the phase transition in materials based on Sb–Te as a function of temperature [16, 25] and composition changes [22] are investigated.

In the context of these applications, it is of interest to study the processes of crystallization in amorphous Sb_2Te films in the context of temperature and impact of an electron beam.

Studying the effect of temperature and sample thickness on the crystallization process will allow us to evaluate the thermal and mechanical resistance of finished devices. Also, indirectly, one can judge their electrical properties. The proven method of exposure to a beam of a transmission electron microscope (TEM) is applicable both to further experiments and to the development of industrial methods.

2. Materials and experimental methods

The samples were synthesized by the group led by Professor M. Wüttig at RWTH Aachen University (Germany). The samples were gradient films (in the order of hundreds of microns) of Sb_2Te deposited on carbon-coated grids via magnetron sputtering. The thickness gradient in the samples was created using a shading plate. Shortly after synthesis, the samples were subjected to vacuum annealing at various temperatures and times. According to the energy-dispersive X-ray spectroscopy, the specimens retain the nominal chemical composition throughout the area.

In this work, the following goals were set. Firstly, the study seeks to investigate patterns of crystallization in thin films along the thickness gradient, depending on the type of exposure, time and annealing temperature. Secondly, the study will determine the features of the formed crystal structures: the phase composition and the main crystallographic orientations.

Sb_2Te samples were studied via transmission electron microscopy on JEOL JEM-2100. According to the analysis of zone-axial patterns (ZAP) in the samples and the interpretation of the corresponding electron diffraction patterns (examples are shown in Figure 1), crystallographic orientations of the antimony phase predominate in the crystallized films (ASTM 05-0562, trigonal syngony, space group $R\bar{3}m$). According to the measurements of the secondary diffraction maxima in the dark field mode [26], the thickness of the crystallized film varies along the gradient from about 15–20 nm to 40–50 nm over several tens of micrometers.

3. Results and Discussion

The Sb_2Te 145C-60s sample was annealed at 145 °C for 60 seconds. In the thinnest area of the thickness gradient, the film is predominantly amorphous (Figure 2a). Along the thickness gradient, the substance crystallizes into separate island-crystallization centers, often with a hexagonal faceting motif, ranging in size from 0.4 μm at the beginning of the thickness gradient to 2 μm in the thickest region. The initial amorphous film's strong relief, which is characteristic of magnetron sputtering, is ignored by crystallization. As we move along the thickness gradient, the size and number of such islands increases. They fill an increasing area of the film and merge, forming a continuous crystalline field (Figure 2c, d). The TEM images do not show a connection between crystallization centers and any defects or features of the film relief. In the film's thickest region, the crystallites measure 1–2.5 μm .

The Sb_2Te 145C-48s sample is similar to the 145C-60s in terms of the morphology, sizes and observed zone-axial patterns of the formed crystallites; therefore, a detailed study was not carried out. The sizes of the crystallites range from 0.2 μm at the beginning of the thickness gradient to 2.8 μm in the thickest region. A small change in the annealing time did not significantly affect the formed crystal structure.

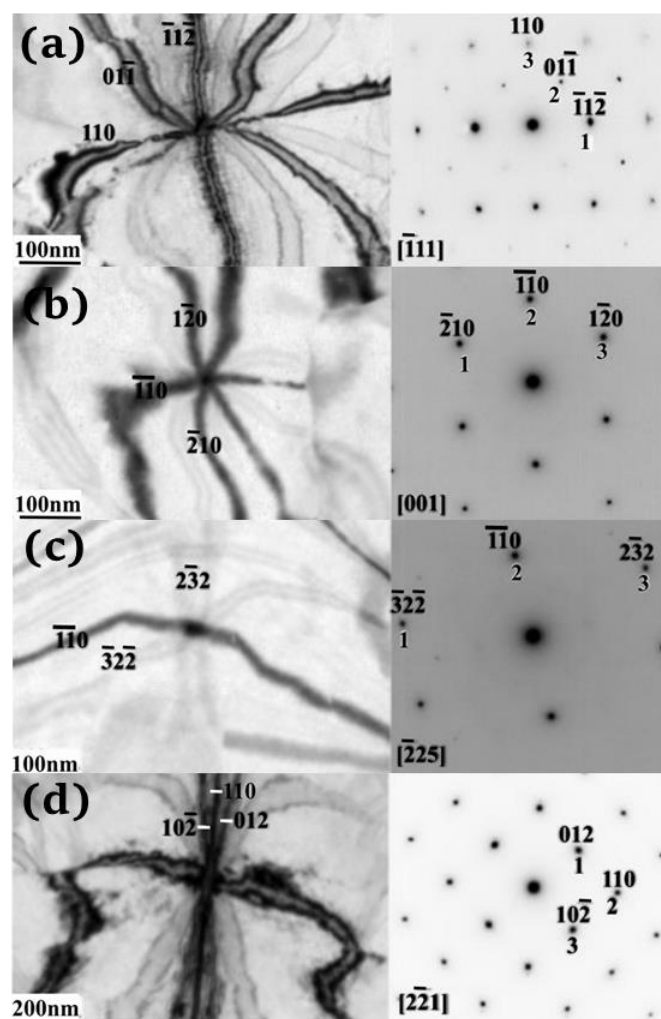


Figure 1 Samples Sb_2Te and (145C-48s (a) and 145C-60s (b, c, d)) ZAP (left), the corresponding indexed electron diffraction patterns of the selected area (right). a - ZAP with zone axis orientation $[\bar{1}11]$ (a); ZAP with orientation $[001]$ (b); ZAP $[225]$; d - ZAP $[2\bar{2}1]$ (c).

The Sb_2Te 120C-90m sample was annealed at 120 °C for 1.5 hours. The pattern of crystallization before the formation of a continuous film was similar to Sb_2Te 145C-48s and Sb_2Te 145C-60s - hexagonal crystalline islands of increasing size and density along the thickness gradient (Figure 3a–c). In the thinnest area, the crystal sizes ranged from 100 to 700 nm. In the thickest continuous film, the crystallites measured 1–3 μm . In the Sb_2Te 120C-90m sample, the largest crystals were observed in the thickest region.

The Sb_2Te 200C-48s sample was annealed at 200 °C for 48 seconds. In this sample, the crystallization processes along the thickness gradient differ from those in the Sb_2Te 145C-48s, Sb_2Te 145C-60s and Sb_2Te 145C-90m samples. Near the phase boundary, the film crystallizes into a homogeneous fine-grained field (Figure 4a, b), with crystal sizes ~10–50 nm. As the thickness of the film increases, the sizes of the crystallites grow, and there are no areas of the amorphous phase between them (Figure 4c, d). This indicates that nucleation in the film increases as annealing temperature increases. This process is enhanced as the sample thickness decreases. The crystallites in the thickest region measure 0.3–1.8 μm , smaller than in the previously considered samples.

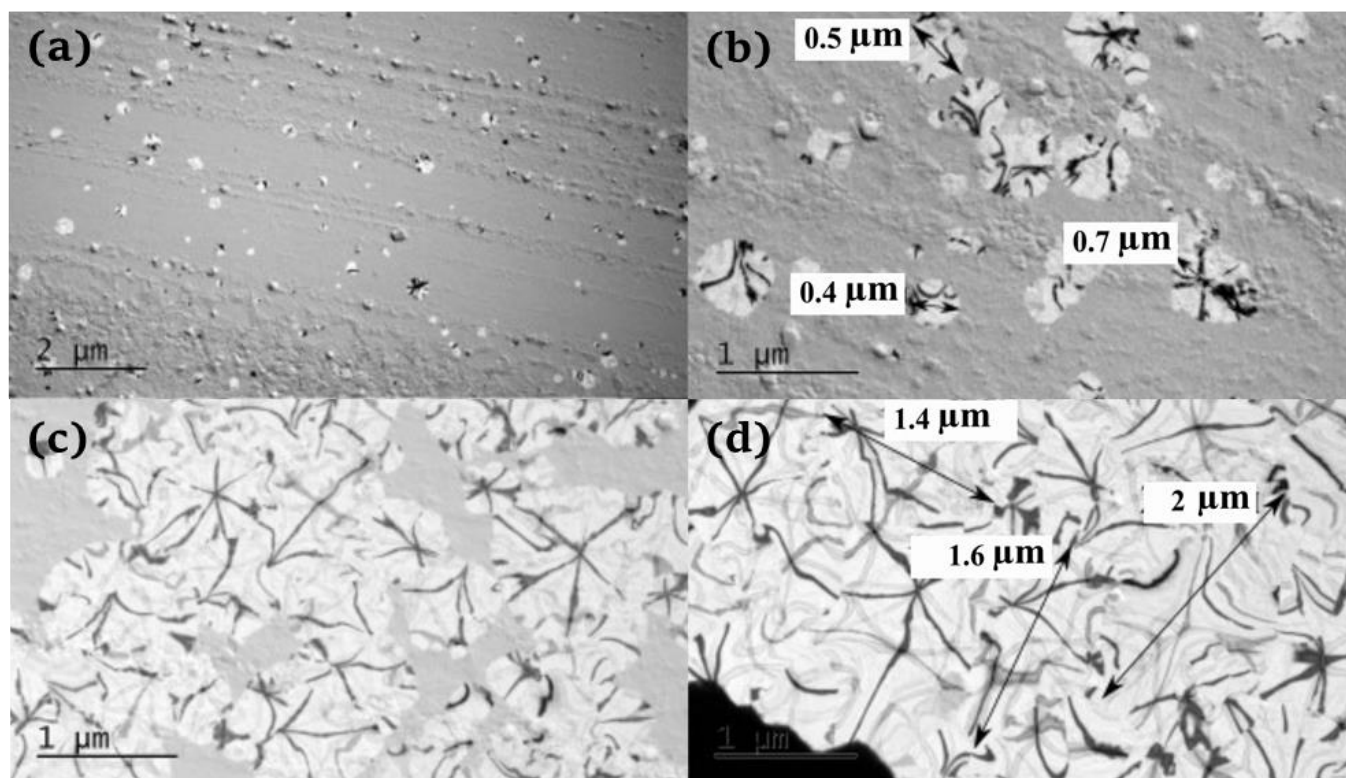


Figure 2 TEM images of the 145C-60s sample at the beginning of the thickness gradient, with a noticeable relief of the initial amorphous film and small crystallites in the amorphous matrix (a, b); image taken from the middle of the gradient, crystalline areas are adjacent to amorphous ones (c); image of a completely crystallized area in the thickest area. Figure 1b, d provides the measurements of some crystallites (d).

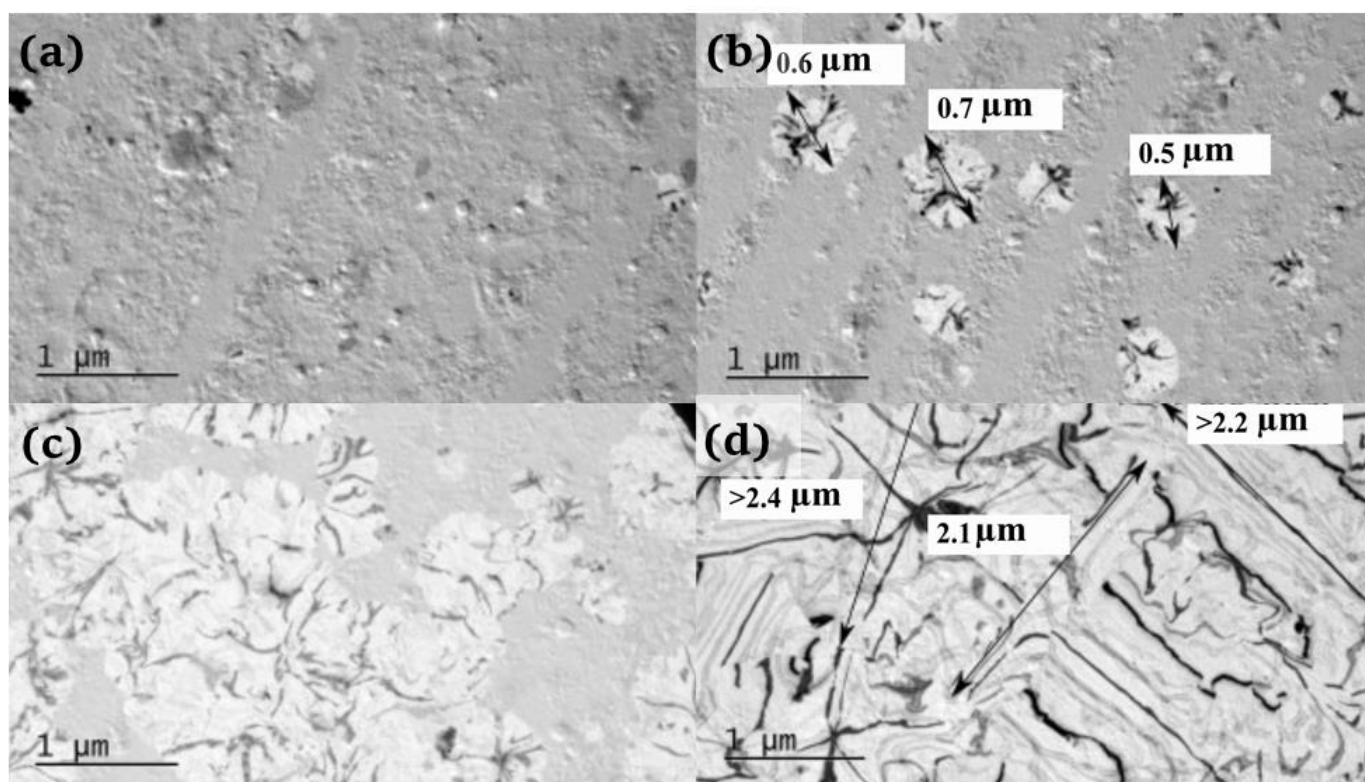


Figure 3 TEM images of the 120C-90m sample at the beginning of the thickness gradient (successively upwards), with individual small/medium crystals in an amorphous matrix (a, b); image of the sample in the area from the middle of the gradient (c); image of the sample in the thickest region. Figure 3b, d show the measurements of the linear dimensions of some crystallites (d).

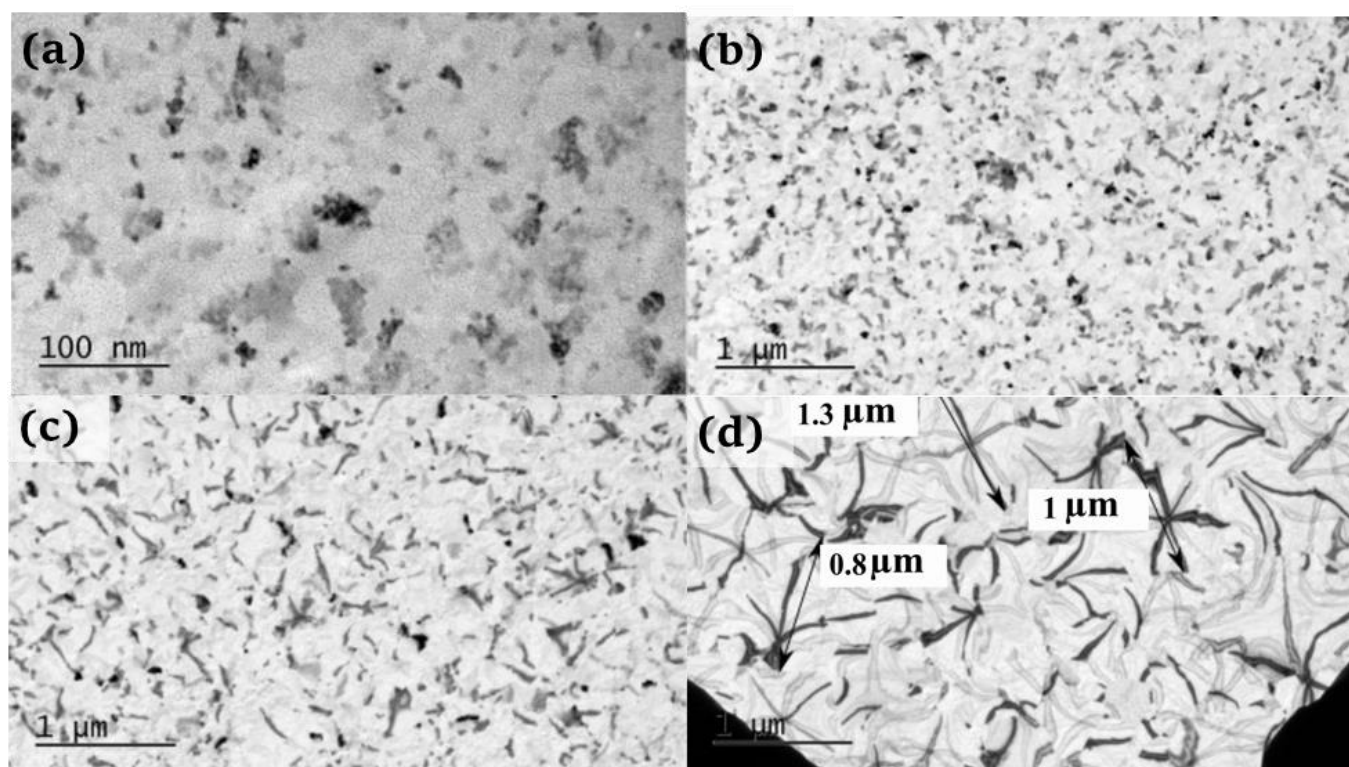


Figure 4 Image of the thinnest area of the 200C-48s sample, individual small crystals are distinguishable (a); images from the gradient's middle (in the direction of increasing thickness) (b, c); image from the thickest region (crystallites reach their maximum size) (d).

In the samples 120C-90m, 145C-60s and 145C-48s, the growth of individual crystals with a hexagonal faceting motif was observed. The general trend of crystallization is an increase in crystal size as the film thickness increases. Changing the annealing conditions affected the crystallized films' morphology. With an increase in annealing time, an increase in the linear dimensions of the crystallites was observed: the largest crystals are observed for the 120C-90m sample annealed for 1.5 hours. An increase in annealing temperature led to the growth of smaller crystals. In the sample annealed at 200 °C, a finely crystalline film was formed in the thinnest region instead of individual crystal nuclei. In the thickest region, the crystallites in this sample were the smallest among all the samples. This indicates an increase in nucleation as annealing temperature increases and film thickness decreases. The authors of [27] indicate an increase in nucleation (the appearance of many crystallization centers in an amorphous matrix) in chalcogenide films based on Sb_2Te and a decrease in thickness (in experiments with simultaneous heating and exposure to a TEM beam). They call this effect paradoxical: if nucleation crystallization occurs on the sample film's surface, then it should not depend on the thickness. If nucleation develops in the bulk of the sample, then a larger number of crystallization centers should appear in a thicker film.

Higher annealing temperatures were characterized by the growth of smaller crystals throughout the thickness gradient, especially in the thinnest regions. This points to the presence of a nucleation mechanism of crystallization. Longer annealing times and lower temperatures were characterized by the growth of larger crystals (growth

crystallization). This can be explained by the nucleation of a smaller number of crystallization centers at a lower temperature. A time factor of tens of minutes obviously has little or no effect on crystallization. The morphology of the samples with an annealing time of tens of seconds or tens of minutes differs insignificantly. The crystals probably formed within a few seconds. The general trend for the entire group of samples is an increase in the size of the formed crystallites and their density on the film as the thickness increased. Fully crystallized by thermal annealing, the film was paved with crystallites of various sizes and arbitrary shapes. No ordering or separate isolated crystallization centers were observed in the samples. This can be explained by the mutual blocking of the growth of neighboring crystals that arise almost simultaneously from numerous crystallization centers. The sample 48s-200C was also distinguished by the fact that, contrary to the general trend, it had the largest number of crystallization centers on the thinnest part. In the temperature range from 145 °C to 200 °C, there is probably a value at which the effect of temperature begins to prevail over the effect of film thickness on the crystallization of Sb_2Te samples.

All the samples were characterized by the same predominant crystallographic orientations, which was determined by electron diffraction data and observed ZAP - $[\bar{1}11]$, $[001]$, $[\bar{2}25]$, $[2\bar{2}1]$, $[122]$. According to the interpretation of the electron diffraction patterns, the substance crystallized in a phase isomorphic to that of antimony. This phenomenon is characteristic of chalcogenide compounds. In the case of antimony-based materials, this is usually the antimony phase. Here, this phase's lower crystallization temperature

may have an effect [28]. The percentage of elements can also play a role. Such is the case for Bi–Sb films with a predominance of bismuth, which crystallize in the bismuth phase [29]. This may mean that there is a lower Sb–Sb binding energy (similar to In–Sb [30]), although other factors may be responsible.

An amorphous Sb_2Te film was exposed to a focused electron beam in a microscope column (Figure 5). The exposure was carried out for 1 min at an accelerating voltage of 200 kV and a beam of maximum intensity (without considering the diaphragms in the TEM column). The current density on the sample was about 10 MA/m^2 . As a result, in the initially amorphous film (Figure 5a), a polycrystalline region with a diameter of about $1 \mu\text{m}$ was formed (Figure 5b, c). An increase in the size of crystallites in the radial direction from the center was observed. Examination of the obtained ring electron diffraction pattern (Figure 6, Table 1) revealed crystallization in the antimony phase. A number of weak reflections in the electron diffraction pattern (Table 1, nos. 10–13) were not correlated with antimony, tellurium or antimony telluride phases. They correspond to small interplanar distances, no data on which are available for these substances from the databases of ASTM X-ray diffraction analysis.

4. Limitations

For further studies, it is necessary to prepare a series of samples with a fixed annealing temperature step. A more accurate assessment of the thermal effect on the sample of the TEM electron beam will also be useful. The currently available equipment also allows simultaneous exposure to an electron beam and heating of the sample substrate *in situ*.

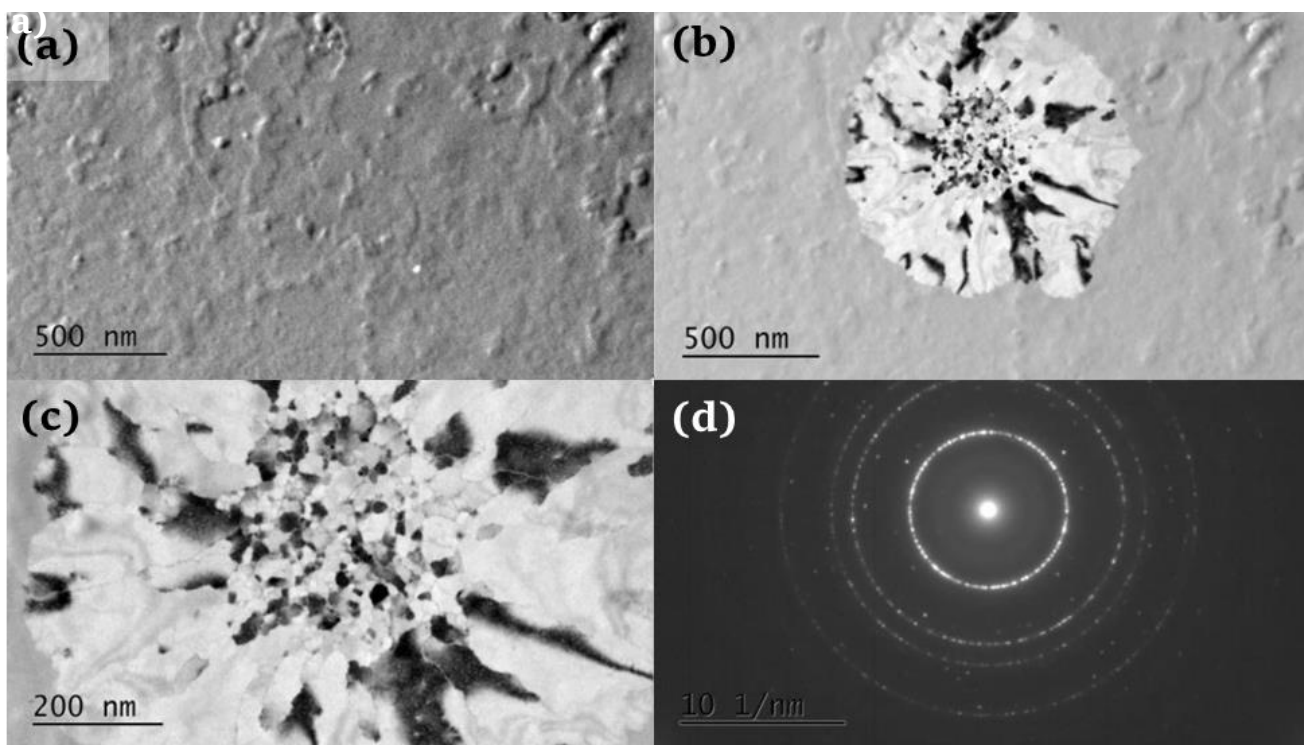


Figure 5 TEM of a section of an amorphous film before exposure to an electron beam (a); TEM of the area after exposure to a focused electron beam (b); crystal structure grown in an amorphous matrix under the action of a beam (c); electron diffraction pattern from the structure in Figure 5c (d).

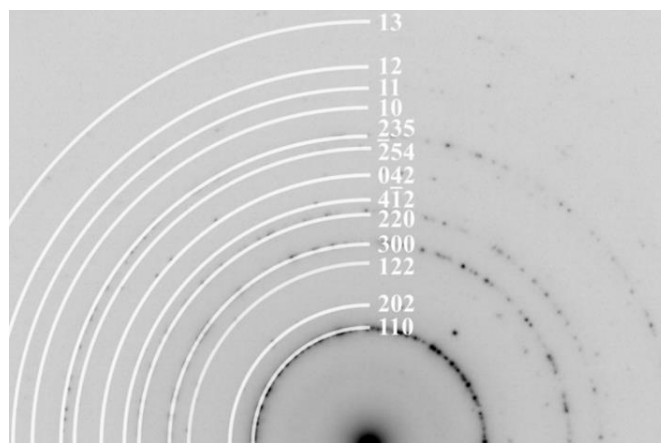


Figure 6 Electron diffraction pattern of the area exposed to an electron beam in the Sb_2Te sample. White arcs with three-digit indices indicate ring reflections associated with the antimony phase; the arcs numbered 10–13 denote unidentified reflections. See Table 1 for the measurement and indication results.

5. Conclusions

Due to annealing, the samples crystallized from the amorphous state. In gradient Sb_2Te samples subjected to vacuum annealing, crystallization is observed to depend both on the film thickness and temperature. As the thickness of the sample increases, the size of the crystals growing in the film enlarges. As the temperature increases, the number of crystals in the film grows. Also, with increasing temperature, the thickness at which crystallization is possible decreases. During thermal crystallization, the processes of nucleation and crystal growth proceed competitively. No spontaneous crystallization was observed in the graded Sb_2Te samples.

Table 1 Identification of antimony phase reflections on the ring electron diffraction pattern from a Sb₂Te sample after exposure to an electron beam (Figure 6).

No. of ring	D, 1/nm	d _{measured} , Å	Observed intensity, %	d _{theor} , Å	Intensity theor., %	hkl
1	9.43	2.12	100	2.15	37	110
2	11.3	1.77	5	1.77	19	202
3	14.92	1.34	5	1.37	16	122
4	16.45	1.22	40	1.24	6	300
5	18.9	1.06	30	1.08	4	220
6	19.87	1.01	10	1.02	7	4-12
7	22.07	0.91	10	0.92	3	042
8	24.01	0.83	10	0.82	9	-254
9	24.95	0.8	30	0.8	4	235
10	28.12	0.71	5			
11	28.71	0.7	5			
12	30.5	0.66	5			
13	33.82	0.59	5			

Crystallization occurred during thermal annealing or exposure to a TEM beam. All the samples crystallized in a phase isomorphic to that of antimony.

The character of crystallization of a magnetron-sputtered Sb₂Te film via a maximum intensity beam differs significantly from that in thermal crystallization. Crystallization under the action of an electron beam is characterized by the formation of polycrystalline regions according to the nucleation mechanism.

In contrast to single crystals, a polycrystalline region is formed corresponding to the area of the beam impact. In the center of the region with a diameter of about 300 nm, where the highest intensity of the TEM beam was achieved, crystallites up to tens of nanometers in size are observed. This points to the nucleation mechanism of crystallization, i.e., the simultaneous nucleation of many neighboring crystallization centers. Outside the central region, much larger crystallites are visible, hundreds of nanometers in size, elongated in the radial direction from the center of the crystallization region. This points to the growth crystallization mechanism, i.e., the growth of the crystalline phase from individual crystallization centers located along the nucleation region's outer edge.

• Supplementary materials

No supplementary materials are available.

• Funding

This work was supported by Russian Foundation for Basic Research (grant no. 20-02-00906), www.rfbr.ru/rffi/eng.

Financial support was provided by the Public Task of the Ministry of Science and Higher Education FEUZ 2023-0020.

• Acknowledgments

The authors are grateful to Professor M. Wüttig for providing the samples for the study.

• Author contributions

Conceptualization: V.Yu.K., A.A.Y.

Data curation: A.A.Y.

Formal Analysis: A.A.Y.

Funding acquisition: V.Yu.K.

Investigation: A.A.Y.

Methodology: V.Yu.K., A.A.Y.

Project administration: V.Yu.K.

Supervision: V.Yu.K.

Validation: V.Yu.K.

Visualization: A.A.Y.

Writing – original draft: A.A.Y.

Writing – review & editing: A.A.Y.

• Conflict of interest

The authors declare no conflict of interest.

• Additional information

Author IDs:

Anton A. Yushkov, Scopus ID [57193951559](https://orcid.org/0009-0001-5719-3951);

Vladimir Yu. Kolosov, Scopus ID [7005960289](https://orcid.org/0009-0001-7005-9602).

Website:

Ural Federal University, <https://urfu.ru/en>.

References

- Xiao Z, Kisslinger K, Dimasi E, Kimbrough J. The fabrication of nanoscale Bi₂Te₃/Sb₂Te₃ multilayer thin film-based thermoelectric power chips. *Microelectron Eng.* 2018;197:8–14. doi:[10.1016/j.mee.2018.05.001](https://doi.org/10.1016/j.mee.2018.05.001)
- Champier D. Thermoelectric generators: A review of applications. *Energy Convers Manag.* 2017;140:167–181. doi:[10.1016/j.enconman.2017.02.070](https://doi.org/10.1016/j.enconman.2017.02.070)
- Vieira EFM, Figueira J. Enhanced thermoelectric properties of Sb₂Te₃ and Bi₂Te₃ films for flexible thermal sensors. *J Alloys Compd.* 2019;774:1102–1116. doi:[10.1016/j.jallcom.2018.09.324](https://doi.org/10.1016/j.jallcom.2018.09.324)
- Haidar SA, Gao Y. Deposition and fabrication of sputtered bismuth telluride and antimony telluride for microscale

- thermoelectric energy harvesters. *Thin Solid Films*. 2021;717:138444(1–9). doi:[10.1016/j.tsf.2020.138444](https://doi.org/10.1016/j.tsf.2020.138444)
5. Voraud A, Seetawan T, Kumar M. Experimental and theoretical study of the thermoelectric properties of rhombohedral $\text{GeSb}_5\text{Te}_{10}$ thin films. *MSEB*. 2019;250:114439(1–5). doi:[10.1016/j.mseb.2019.114439](https://doi.org/10.1016/j.mseb.2019.114439)
 6. Ding X, Yang X. Theoretical analysis and simulation of a tunable mid-infrared filter based on $\text{Ge}_2\text{Sb}_2\text{Te}_5$ (GST) metasurface. *Superlattices Microstruct*. 2019;132:106169(1–6). doi:[10.1016/j.spmi.2019.106169](https://doi.org/10.1016/j.spmi.2019.106169)
 7. Cheng L, Yuan Y. Linear and nonlinear optical properties modulation of $\text{Sb}_2\text{Te}_3/\text{GeTe}$ bilayer film as a promising saturable absorber. *Results Phys*. 2019;13:102282(1–7). doi:[10.1016/j.rinp.2019.102282](https://doi.org/10.1016/j.rinp.2019.102282)
 8. Khusayfan, N. M. and Khanfar H. K. Characterization of $\text{CdS}/\text{Sb}_2\text{Te}_3$ micro/nano-interfaces. *Optik*. 2018;158:1154–1159. doi:[10.1016/j.ijleo.2018.01.010](https://doi.org/10.1016/j.ijleo.2018.01.010)
 9. Liu G, Wu L. The investigations of characteristics of Sb_2Te as a base phase-change material. *Solid State Electron*. 2017;135:31–36. doi:[10.1016/j.sse.2017.06.004](https://doi.org/10.1016/j.sse.2017.06.004)
 10. Liu B, Song Z, Feng S, Chen B. Characteristics of chalcogenide nonvolatile memory nano-cell-element based on Sb_2Te_3 material. *Microelectron Eng*. 2005;82(2):168–174. doi:[10.1016/j.mee.2005.07.007](https://doi.org/10.1016/j.mee.2005.07.007)
 11. Ding K, Chen B, Rao F. Boosting crystallization speed in ultrathin phase-change bridge memory device using Sb_2Te_3 . *Mater Sci Semicond Process*. 2021;136:105999(1–6). doi:[10.1016/j.mssp.2021.105999](https://doi.org/10.1016/j.mssp.2021.105999)
 12. Hu J, Lin C. Cr-doped Sb_2Te materials promising for high performance phase-change random access memory. *J Alloys Compd*. 2022;908:164593. doi:[10.1016/j.jallcom.2022.164593](https://doi.org/10.1016/j.jallcom.2022.164593)
 13. Wang G, Shen X. Improved thermal stability of C-doped Sb_2Te films by increasing degree of disorder for memory application. *Thin Solid Films*. 2016;615:345–350. doi:[10.1016/j.tsf.2016.07.059](https://doi.org/10.1016/j.tsf.2016.07.059)
 14. Yang C-H, Chiang K-C, Hsieh T-E. Nonvolatile floating gate memory characteristics of $\text{Sb}_2\text{Te}-\text{SiO}_2$ nanocomposite thin films. *Thin Solid Films*. 2013;529:263–268. doi:[10.1016/j.tsf.2012.07.135](https://doi.org/10.1016/j.tsf.2012.07.135)
 15. Liu F, Wang G, Zhang Y, Li C. Improved multi-level storage performance by insulator-metal transition of In_2S_3 -doped $\text{Ge}_2\text{Sb}_2\text{Te}_5$ films. *Ceram*. 2019;45:24090–24095. doi:[10.1016/j.ceramint.2019.08.116](https://doi.org/10.1016/j.ceramint.2019.08.116)
 16. Lotnyk A, Hilmi I, Behrens M, Rauschenbach B. Temperature dependent evolution of local structure in chalcogenide-based superlattices. *Appl Surf Sci*. 2021;536:147959(1–8). doi:[10.1016/j.apsusc.2020.147959](https://doi.org/10.1016/j.apsusc.2020.147959)
 17. Jiang K, Lu Y. $\text{GeTe}/\text{Sb}_4\text{Te}$ films: A candidate for multilevel phase change memory. *MSEB*. 2018;231:81–85. doi:[10.1016/j.mseb.2018.10.002](https://doi.org/10.1016/j.mseb.2018.10.002)
 18. Kampmeier J, Weyrich C. Selective area growth of Bi_2Te_3 and Sb_2Te_3 topological insulator thin films. *J Cryst Growth*. 2016;443:38–42. doi:[10.1016/j.jcrysgro.2016.03.012](https://doi.org/10.1016/j.jcrysgro.2016.03.012)
 19. Bera S, Behera P. Weak antilocalization in Sb_2Te_3 nano-crystalline topological insulator. *Appl Surf Sci*. 2019;496:143654(1–6). doi:[10.1016/j.apsusc.2019.143654](https://doi.org/10.1016/j.apsusc.2019.143654)
 20. Buga SG, Kulbachinskii VA. Superconductivity in bulk polycrystalline metastable phases of Sb_2Te_3 and Bi_2Te_3 quenched after high-pressure-high-temperature treatment. *Chem Phys Lett*. 2015;631:97–102. doi:[10.1016/j.cplett.2015.04.056](https://doi.org/10.1016/j.cplett.2015.04.056)
 21. Choi M, Choi H, Ahn J, Kim YT. Material design for $\text{Ge}_2\text{Sb}_2\text{Te}_5$ phase-change material with thermal stability and lattice distortion. *Scr Mater*. 2019;170:16–19. doi:[10.1016/j.scriptamat.2019.05.024](https://doi.org/10.1016/j.scriptamat.2019.05.024)
 22. Nolot E, Sabbione C, Germanium, antimony, tellurium, their binary and ternary alloys and the impact of nitrogen: An X-ray photoelectron study. *Appl Surf Sci*. 2021;536:147703(1–21). doi:[10.1016/j.apsusc.2020.147703](https://doi.org/10.1016/j.apsusc.2020.147703)
 23. Peng L, Li Z. Reduction in thermal conductivity of Sb_2Te phase-change material by scandium/yttrium doping. *J Alloys Compd*. 2020;821:153499(1–7). doi:[10.1016/j.jallcom.2019.153499](https://doi.org/10.1016/j.jallcom.2019.153499)
 24. Meng Y, She Q. Uniform silicon carbide doped Sb_2Te nano-material for high temperature and high speed PCM applications. *J Alloys Compd*. 2016;664:591–594. doi:[10.1016/j.jallcom.2016.01.036](https://doi.org/10.1016/j.jallcom.2016.01.036)
 25. Pandey SK, Manivannan A. Direct evidence for structural transformation and higher thermal stability of amorphous InSbTe phase change material. *Scr Mater*. 2021;192:73–77. doi:[10.1016/j.scriptamat.2020.10.014](https://doi.org/10.1016/j.scriptamat.2020.10.014)
 26. Delavignette P, Vook RW. Method for measuring the thickness of thin bent foils in transmission electron microscopy. *Phys Stat Sol*. 1963;3:648–653. doi:[10.1002/pssb.19630030406](https://doi.org/10.1002/pssb.19630030406)
 27. Kooi BJ, De Hosson ThM. On the crystallization of thin films composed of $\text{Sb}_{3.6}\text{Te}$ with Ge for rewritable data storage. *J Appl Phys*. 2004;95(9):4714–4721. doi:[10.1063/1.1690112](https://doi.org/10.1063/1.1690112)
 28. Song SA, Zhang W, Jeong HS, Kim J-G, Kim Y-J. *In situ* dynamic HR-TEM and EELS study on phase transitions of $\text{Ge}_2\text{Sb}_2\text{Te}_5$ chalcogenides. *Ultramicroscop*. 2008;108. doi:[10.1016/j.ultramic.2008.05.012](https://doi.org/10.1016/j.ultramic.2008.05.012)
 29. Ryu H, You Y, Paek MC, Kang K. Microscopic behavior of Sb in chalcogenide materials for crystallization process. *Mater Sci Eng A*. 2007;449:573–577. doi:[10.1016/j.msea.2006.02.421](https://doi.org/10.1016/j.msea.2006.02.421)
 30. Kim YT, Kim ET, Kim CS, Lee JY. Phase transformation mechanism of In–Sb–Te through the boundary reaction between InSb and InTe . *Phys Stat Sol*. 2011;5(3):98–100. doi:[10.1002/pssr.201004515](https://doi.org/10.1002/pssr.201004515)